Progress in Applied CFD

SINTEF

SINTEF Proceedings

Editors:
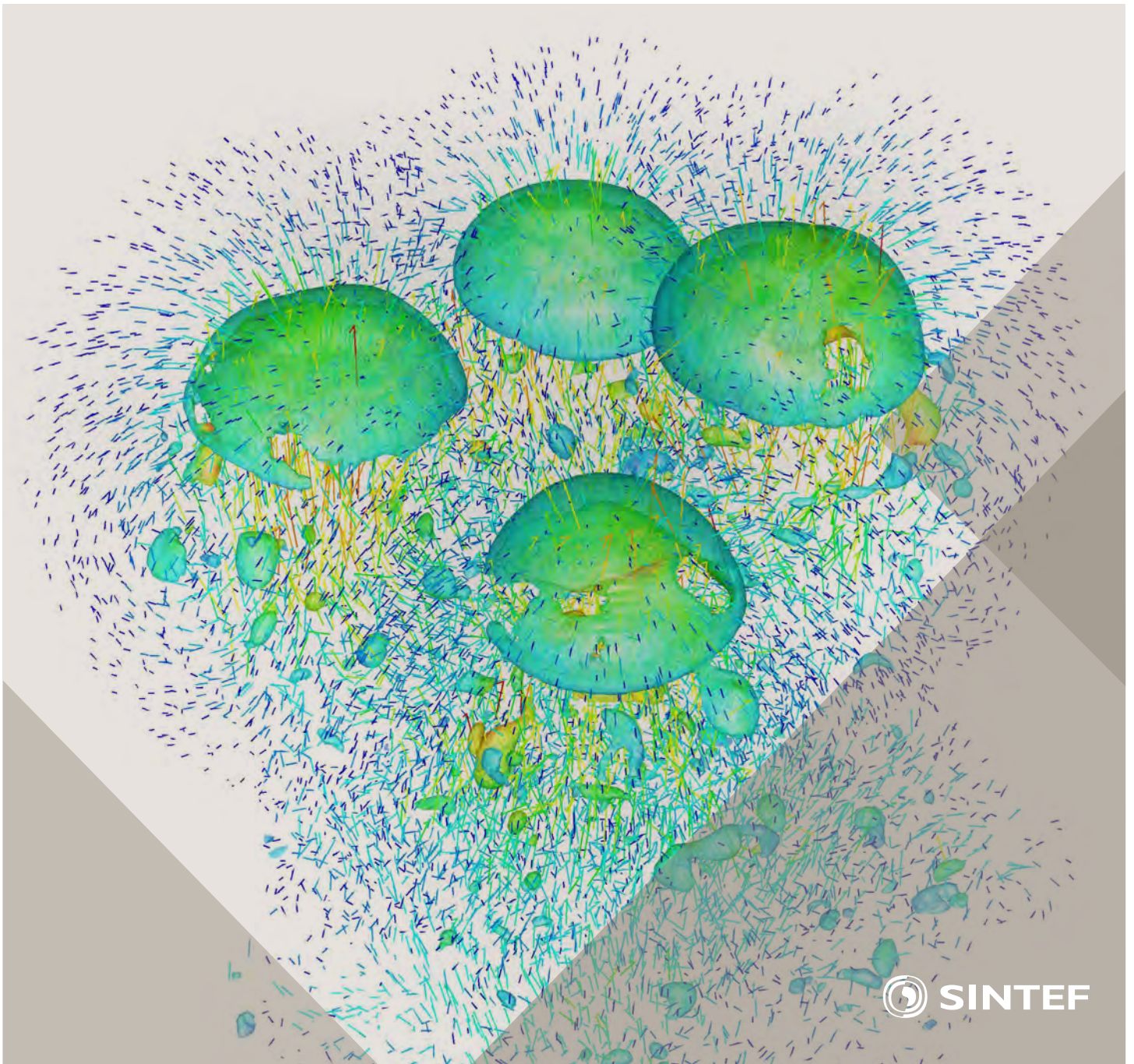Jan Erik Olsen and Stein Tore Johansen

Progress in Applied CFD

Selected papers from 10th International Conference on Computational Fluid
Dynamics in the Oil & Gas, Metallurgical and Process Industries

SINTEF Academic Press

SINTEF Proceedings
SINTEF Proceedings is a serial publication for peer-reviewed conference proceedings
on a variety of scientific topics.
The processes of peer-reviewing of papers published in SINTEF Proceedings are
administered by the conference organizers and proceedings editors. Detailed procedures
will vary according to custom and practice in each scientific community.

PREFACE

This book contains selected papers from the 10th International Conference on Computational Fluid Dynamics in the Oil & Gas, Metallurgical and Process Industries. The conference was hosted by SINTEF in Trondheim in June 2014 and is also known as CFD2014 for short. The conference series was initiated by CSIRO and Phil Schwarz in 1997. So far the conference has been alternating between CSIRO in Melbourne and SINTEF in Trondheim. The conferences focus on the application of CFD in the oil and gas industries, metal production, mineral processing, power generation, chemicals and other process industries. The papers in the conference proceedings and this book demonstrate the current progress in applied CFD.

The conference papers undergo a review process involving two experts. Only papers accepted by the reviewers are presented in the conference proceedings. More than 100 papers were presented at the conference. Of these papers, 27 were chosen for this book and reviewed once more before being approved. These are well received papers fitting the scope of the book which has a slightly more focused scope than the conference. As many other good papers were presented at the conference, the interested reader is also encouraged to study the proceedings of the conference.

The organizing committee would like to thank everyone who has helped with paper review, those who promoted the conference and all authors who have submitted scientific contributions. We are also grateful for the support from the conference sponsors: FACE (the multiphase flow assurance centre), Total, ANSYS, CD-Adapco, Ascomp, Statoil and Elkem.

Stein Tore Johansen & Jan Erik Olsen

3

CONTENTS

AN ENHANCED FRONT TRACKING METHOD FEATURING VOLUME CONSERVATIVE REMESHING AND MASS TRANSFER

Ivo ROGHAIR[1][*], **Martin VAN SINT ANNALAND**[1][†], **Hans KUIPERS**[2][‡]

[1]Chemical Process Intensification, Multiphase Reactors Group, Eindhoven University of Technology,

The Netherlands

[2]Multiscale Modeling of Multiphase Flows, Multiphase Reactors Group, Eindhoven University of

Technology, The Netherlands

[*] E-mail: i.roghair@tue.nl
[†] E-mail: m.v.sintannaland@tue.nl
[‡] E-mail: j.a.m.kuipers@tue.nl

ABSTRACT

A chemical species transport model is developed and coupled to an improved Front-Tracking model, enabling dynamic simulation of gas-liquid mass transfer processes in dense bubbly flows. Front-Tracking (FT) is a multiphase computational fluid dynamics technique where the location of a fluid-fluid interface is tracked via the advection of interface marker points, which make up a triangular mesh. A common drawback of FT implementations is that the volume enclosed by a mesh is not conservative during transient simulations. A remeshing technique is adopted to counteract these volume defects while keeping all physical undulations unharmed. The new remeshing procedures have been verified by comparison with results from the literature.

Species transport is modelled by a convection-diffusion equation which is discretized on a Eulerian grid, superimposed and possibly refined with respect to the grid used for the solution of the fluid flow equations. The velocity components have been interpolated to the refined grid using a higher-order solenoidal method. Enforcement of the Dirichlet condition for the concentration at the gas-liquid interface is achieved with an immersed boundary method, enabling the description of gas to liquid mass transfer. Careful validation of the newly implemented model, using synthetic benchmarks (exact solutions) and a comparison with correlations from the literature, has shown satisfactory results.

The model is used for a variety of hydrodynamic studies. In particular, the model is very suited to simulate (dense) bubbly flows due to the absence of artificial coalescence. A number of results, such as a closure of the drag force for bubbles rising in a bubble swarm and simulations of the bubble-induced turbulent energy spectra will be outlined.

The liquid side mass transfer coefficient in dense bubble swarms, with gas fractions between 4% and 40%, has been investigated using the new model. The simulations have been performed in a 3D domain with periodic boundaries, mimicking an infinite swarm of bubbles. To prevent the liquid phase to become saturated with chemical species (with the consequence of a vanishing chemical species flux due to saturation of the liquid bulk), simulations have been performed using either artificial fresh liquid inflow, or a first order chemical reaction in the liquid phase. The results indicate that the liquid-side mass transfer coefficient rises slightly with increasing gas fraction.

Keywords: CFD, hydrodynamics, bubbly flows, turbulence, mass transfer .

NOMENCLATURE

Greek Symbols

α Gas hold-up, [-].
Γ Solution grid, [-].
ϕ Volume fraction, [-].
ρ Mass density, [kg/m^3].
μ Dynamic viscosity, [Pa s].
σ Surface tension, [N/m].
χ Aspect ratio, [-].

Latin Symbols

A, S Surface, [m^2].
c   Centroid, [m].
c Concentration, [mol/L].
C_D Drag coefficient, [-].
d Diameter, [m].
$\mathscr{D}$ Diffusion coefficient, [m^2/s].
Eo   Eötvös numer Eo $= \frac{gd^2\rho}{\sigma}$, [-].
F Force, [N].
g Gravity constant, [m/s^2].
H Henry's constant, [-].
k_L Mass transfer coefficient, [m/s].
p Pressure, [Pa].
Pe   Péclet number Pe $= \frac{v_\infty d}{\mathscr{D}}$, [-].
Re   Reynolds number Re $= \frac{\rho|\mathbf{u}|d}{\mu}$, [-].
Sh   Sherwood number Sh $= \frac{k_L d}{\mathscr{D}}$, [-].
n   Normal, [-].
t   Tangent, [-].
t Time, [s].
u   Velocity, [m/s].
V Volume, [m^3].

Sub/superscripts

a, b, c, i, m Marker indicator.
h, s Hydrodynamic/Species mesh.
b Bubble.
$n, *, n+1$ Previous, intermediate, next (time step).
∞ Single rising bubble in a quiescent liquid.

INTRODUCTION

In the chemical industry, many processes involve the exchange of (possibly reacting) components between a gas and liquid phase, for instance in oxidation or hydrogenation processes (Deen *et al.*, 2010). Such processes are typically per-

formed in bubble column (slurry) reactors, a column filled with liquid (and possibly a solid catalyst) in which gaseous reactants are introduced at the bottom or via immersed spargers. The gas flow rate is usually large so that dense bubble swarms rise through the liquid.

In order to understand and optimize these processes, it is important to gain insight in the the hydrodynamic and mass transfer characteristics of bubbles rising in a swarm. In recent work, we have used direct numerical simulations (DNS) to study the drag acting on bubbles rising in a swarm (Roghair *et al.*, 2011b), and the resulting closure relations have successfully been applied in a (larger scale) discrete bubble model (Lau *et al.*, 2011). The use of DNS, as opposed to detailed experiments, has advantages, as it provides full insight in the dynamics of the flow, including the deformation of the interface and the micro-structure of the flow field. Besides studying the drag acting on rising bubbles, the method can be used to describe bubble clustering and bubble induced turbulence, but when a suitable extension with mass transfer equations is provided, it can be used to study the overall mass transfer coefficient k_L in dense bubble swarms. The current work presents a number of hydrodynamic studies that have been performed with the Front Tracking model as well as our recent achievements to obtain the gas-to-liquid mass transfer coefficient for bubbles rising in a swarm. We outline the implementation of the numerical model (hydrodynamics and mass transfer), provide validation of the implementation and evaluate the results.

MODEL DESCRIPTION

The front tracking model used in this work has been in development in our group for about 9 years. The hydrodynamics discretisation and implementation using the Finite Volume Method is also described in detail in Dijkhuizen *et al.* (2010b). In the sections below, the basic routines of the algorithm are described. We want to highlight the renewed remeshing procedures and the incorporation of the mass transfer module.

Hydrodynamics modeling

The governing equations of the fluid flow field are given by the incompressible Navier-Stokes equation and the continuity equation, discretized on a Cartesian coordinate system using a one-fluid formulation:

$$\rho \frac{\partial \mathbf{u}}{\partial t} + \rho \nabla \cdot (\mathbf{u}\mathbf{u}) = -\nabla p + \rho \mathbf{g} + \nabla \cdot \mu \left[\nabla \mathbf{u} + (\nabla \mathbf{u})^T \right] + \mathbf{F}_\sigma$$
(1a)

$$\nabla \cdot \mathbf{u} = 0$$
(1b)

where $\mathbf{u}$ is the fluid velocity and $\mathbf{F}_\sigma$ representing a singular source-term for the surface tension force at the interface. The velocity field is continuous even across interfaces, so a one-fluid formulation has been used. The equations are solved with a finite volume technique using a staggered discretisation (see Figure 1). The flow field is solved using a two-stage projection-correction method. After solving the momentum balance for each velocity component separately, a pressure-correction step is taken to satisfy the continuity equation. These steps use an incomplete Cholesky conjugate gradient (ICCG) method to solve the linearized equations. The boundary conditions can be adjusted between free-slip, no-slip and periodic, but only the latter is used in this work.

Surface mesh

The interface is parameterized by Lagrangian tracking (control) points. The connectivity of the points build up a mesh with triangular cells, called markers (Figure 1). The positions of the control points are updated each time step. After the fluid flow has been calculated, the Lagrangian control points are moved with the interpolated velocity to their new locations (a cubic spline method is used for interpolation). The actual movement is performed using a 4th order Runge-Kutta time stepping scheme.

Surface tension force and pressure jump

In Eq. 1a, $\mathbf{F}_\sigma$ represents the surface tension force, a vector quantity that can be directly calculated from the positions of the interface markers. The individual pull-force of neighbouring marker *i* acting on marker *m* can be computed from their normal vectors and joint tangent as illustrated in Figure 2:

$$\mathbf{F}_{\sigma, i \rightarrow m} = \sigma \left(\mathbf{t}_{mi} \times \mathbf{n}_{mi} \right)$$
(2a)

The shared tangent $\mathbf{t}_{mi}$ is known from the control point locations, and the shared normal vector $\mathbf{n}_{mi}$ is obtained by averaging, from which we can discard one term due to orthogonality:

$$\mathbf{t}_{mi} \times \mathbf{n}_{mi} = \frac{1}{2} \left(\underbrace{(\mathbf{t}_{mi} \times \mathbf{n}_m)}_{=0} + (\mathbf{t}_{mi} \times \mathbf{n}_i) \right)$$
(2b)

Hence, the total surface tension force on a marker *m* is obtained by summing Eq. 2a for all three neighbouring markers:

$$\mathbf{F}_{\sigma, m} = \tfrac{1}{2} \sigma \sum_{i=a,b,c} (\mathbf{t}_{mi} \times \mathbf{n}_i) = \tfrac{1}{2} \sum_{i=a,b,c} \mathbf{F}_{\sigma, i \rightarrow m}$$
(2c)

As a result, three pull forces on each marker are defined which yield a net force inward, opposing the pressure jump.
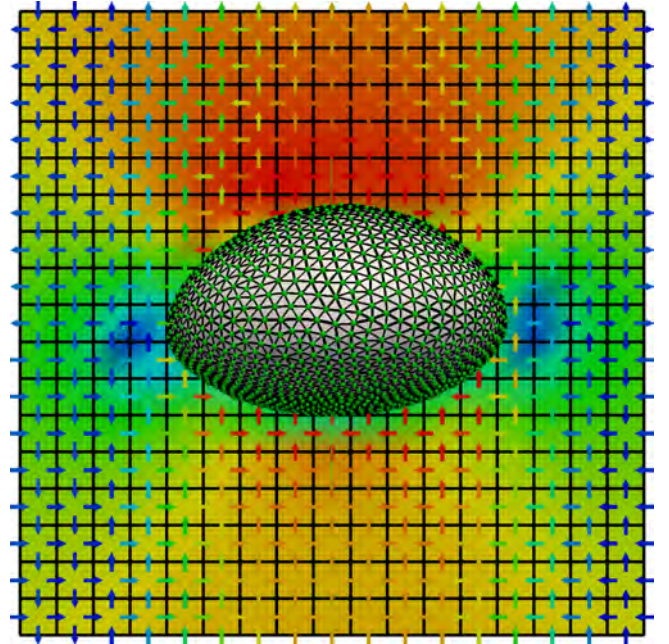

Figure 1: A zoomed snapshot of a rising FT bubble (at a very low resolution for illustration purposes), showing the tracking points and surface mesh, and the background grid with staggered velocity vectors. The colors of the background grid indicate the pressure profile, and the colors of the velocity vectors represent the magnitude.

For a closed surface, the net surface tension force on the entire object will be zero. This force $\mathbf{F}_\sigma$ is then mapped to the Eulerian cells closest to marker m using mass-weighing (Deen *et al.*, 2004) (regularized Dirac function).   An im-
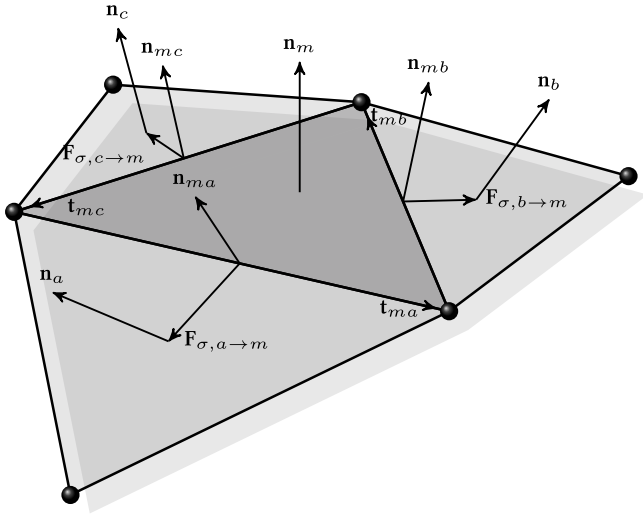

Figure 2: The surface tension calculation on marker involves the calculation of three pull-forces using the tangent and normal vectors shared with the neighbouring marker.

portant aspect of DNS involving small bubbles (e.g. $d_b \leq 1.0$ mm air bubbles in water) is the large pressure jump at the gas-liquid interface, which may cause parasitic currents that may affect the final solution significantly. While these artificial currents are decreased by the mass weighing implementation (explained above), Popinet and Zaleski (1999) demonstrated that the coupling between the surface forces and the pressure jump is crucial to further minimize them. Our approach is outlined in Dijkhuizen *et al.* (2010b). The Front-Tracking model uses a method similar to Renardy and Renardy (2002) and Francois *et al.* (2006), where the pressure forces will be extracted from the surface forces at the interface, only mapping the resulting net force.

First note that the partial pressure drop (i.e. the pressure jump $[p]$ resulting from the surface tension force on a single marker), can be calculated using Eq. 3, if the shear stress in the normal direction is neglected.

$$\int_{\partial S} [p] \, dS = \int_{\partial S} \mathbf{F}_\sigma \cdot \mathbf{n}$$
$$[p] = \frac{\int_{\partial S} \mathbf{F}_\sigma \cdot \mathbf{n}}{\int_{\partial S} dS} = \frac{\sum_m \mathbf{F}_{\sigma,m} \cdot \mathbf{n}_m}{\sum_m S_m} \tag{3}$$

The sum of the surface forces of all markers yields the pressure jump of the bubble as a whole. By distributing the total pressure jump equally back to the Eulerian mesh, the pressure jump is incorporated in the right-hand side of the momentum equations. For interfaces with a constant curvature (i.e. a sphere), the pressure jump and surface tension cancel each other out exactly, and if the curvature varies over the interface, only a relatively small nett force will be transmitted to the Euler grid.

Phase fraction and physical properties

Since the marker positions are exactly known, the phase fraction ϕ in each Eulerian cell can be computed exactly using geometric analysis. With the phase fraction, the density of each Eulerian cell is calculated by weighted averaging. The viscosity is obtained by harmonic averaging of the kinematic viscosities (Prosperetti, 2002):

$$\rho(\mathbf{x}) = \sum_{p=0}^{n_{\text{phase}}-1} \phi_p(\mathbf{x}) \rho_p \tag{4a}$$

$$\frac{\rho(\mathbf{x})}{\mu(\mathbf{x})} = \sum_{p=0}^{n_{\text{phase}}-1} \phi_p(\mathbf{x}) \frac{\rho_p}{\mu_p} \tag{4b}$$

The bubble properties *viz.* total surface area, volume and centroid position, can be efficiently obtained by summing over all triangular markers of an interface n_m. A scale factor s_m is defined, equal to twice the surface area of a marker obtained by the magnitude of the cross product of two marker edges $\mathbf{t}_{ma}$ and $\mathbf{t}_{mb}$:

$$s_m = |\mathbf{t}_{ma} \times \mathbf{t}_{mb}| \tag{5}$$

The total surface area of bubble b is computed with:

$$A_b = \frac{1}{2} \sum_{m=1}^{n_m} s_m \tag{6}$$

The volume of a bubble is obtained using:

$$V_b = \frac{1}{6} \sum_{m=1}^{n_m} s_m (\mathbf{c}_m \cdot \mathbf{n}_m) \tag{7}$$

with $\mathbf{c}_m$ the geometric centre of the marker and $\mathbf{n}_m$ the unit normal vector of the marker. Finally, the bubble centroid follows directly from the centroids of the triangular markers weighted with the surface area:

$$\mathbf{c}_b = \frac{\sum_{m=1}^{n_m} s_m \mathbf{c}_m}{\sum_{m=1}^{n_m} s_m} \tag{8}$$

The bubble velocity is computed from the displacement of the bubble centroid. Also, the bubble diameter along the Cartesian directions can be obtained from the minimum and maximum location of the marker points.

Remeshing

The remeshing procedure is an essential part of the Front-Tracking technique. Due to interface advection, velocity gradients induce surface grid distortion and marker elements become too large or too small, leading to a poor grid quality and in its turn decreased accuracy in the surface tension force computation. To overcome this, the remeshing procedure takes care of local relocation of the points and marker connectivity (topology changes), without "ironing out" physical undulations.

Volume changes

In the Front-Tracking method, the volume enclosed by an interface mesh may change. Although the volume changes per time step are very small, these volume changes may accumulate significantly during a simulation due to the very large number of time steps required (Figure 3) and hence must be prevented (Pivello *et al.*, 2013). Especially for the simulation of bubble swarms, where simulations should last for a longer time than for single rising bubbles, it is essential to prevent such effects. The change in volume can be caused by remeshing operations, such as edge splitting, collapsing, smoothing and swapping and due to the advection of the interface. Bunner and Tryggvason (2002) have proposed to solve this problem by displacing the points with respect to the bubble centroid every 100 time steps in such a way that the volume

of the bubble is identical to the original bubble volume. This might cause problems when the centroid lies outside the actual enclosed volume (*viz.* skirted bubbles). In this work, a remeshing technique was implemented to prevent bubble volume changes, with a minimal impact on the bubble shape.
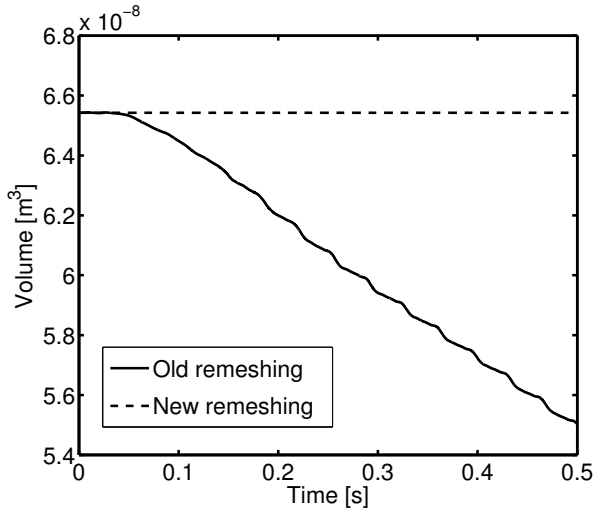

Figure 3: Volume changes may accumulate significantly during a simulation, due to advection of the interface and by using traditional, non volume-conservative remeshing methods. Using a volume-conservative remeshing technique, these effects can be prevented. The figure shows a volume vs time plot of a $d_b = 5.0$ mm air bubble in water, using both the old and new remeshing techniques.

Elementary remeshing operations

The traditional remeshing approach involves edge splitting, collapsing and swapping. In the remeshing technique presented here, these common procedures have been extended with volume conservative smoothing (regularization of the interface markers) as discussed below. Additionally, procedures are required to prevent the occurrence of rare but catastrophic mesh configurations, such as pyramids (tetraeders connected to the mesh by only a single point) or double folded marker cells.

Edge splitting and collapsing An edge is splitted (node addition) or collapsed (node removal) based on the edge length criterium which relates the edge length ℓ_m to the Eulerian cell size h according to $\frac{1}{5}h \leq \ell_m \leq \frac{1}{2}h$. In order to obtain a higher resolution in more deformed regions of the mesh, the local mesh roughness (defined as the minimum dot product of any two adjacent normals of markers connected to a node) is used to shift the balance in this algorithm towards node addition or removal.

Edge swapping In some cases, it is preferable to swap an edge rather than deleting or adding a node to the mesh. Whether or not an edge needs to be swapped depends on the number of connections of the nodes involved. This procedure ensures that equilateral marker cells are preferred.

Smoothing By distributing the control points over the interface, the grid quality can be enhanced and the required frequency of applying the other remeshing algorithms can be strongly decreased. In our algorithm, we have opted for edge-relaxation as explained by (Kuprat *et al.*, 2001).

Volume restoring/conservation

We have implemented a volume restoration/conservation method as described by Kuprat *et al.* (2001) in the Front-Tracking model. Here we present the general idea of the algorithm, the referred work provides more details on its implementation.

Whenever a node is displaced, a volume defect can be obtained by considering the volume for the situation before and after remeshing. The volume is obtained by selecting all marker cells that are connected to that node, and creating several tetrahedra using the three nodes of each marker and the bubble centroid using a scalar triple product. This volume defect can be corrected by shifting edges such that the original volume is restored, while the impact on the actual geometry of the mesh is minimized.

While this technique resolves volume changes due to prescribed point removal, edge swapping or smoothing, any volume changes that may have occurred during mesh advection, however, still need to be restored. Therefore, after the mesh restructuring, the algorithm sweeps over an entire interface mesh at once, distributing any additional volume corrections over the entire interface. This may cause the interfaces of different dispersed elements in very close proximity to cross each other, hence yield non-physical results. If such a situation occurs, the points crossing another interface are moved back and the volume difference is again distributed over all nodes of the interface, excluding those that have been moved back. We use a *k*-dimensional tree (kdtree, Tsiombikas (2009)) to efficiently find any points that may overlap with another interface.

Performance of the new remeshing technique

The complete revision of a cornerstone element such as the remeshing must be thoroughly validated before the code can be used for production runs. We have simulated a $d_b = 4.0$ mm air bubble in water using the old and new technique and compared the interface mesh (Figure 4) and the rise velocity profile as a function of time (Figure 5).
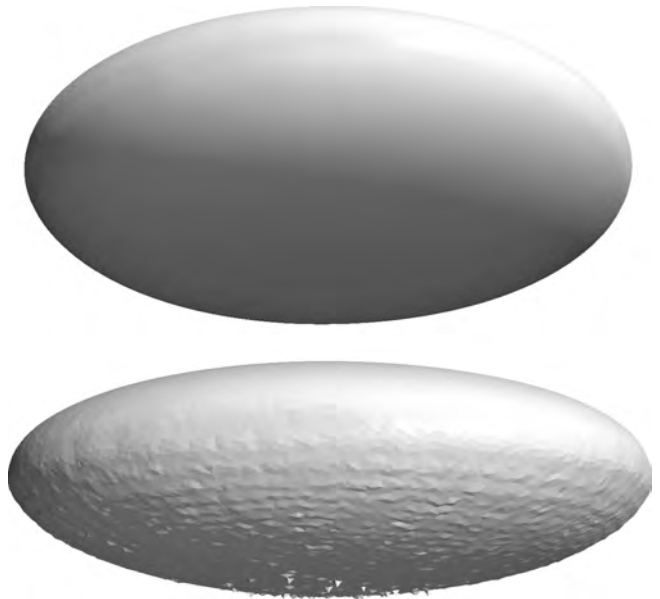

Figure 4: The mesh structure compared for the old and new remeshing techniques. It can be seen that the bubble interface using the old remeshing technique shows profound undulations and artefacts.

The interface mesh is, as expected, much smoother compared to the old remeshing technique. The rise velocity shows a slightly different profile; although both techniques show the onset of the velocity oscillations at the same time (due to the wobbling behaviour of the bubble), the velocity profiles are out of phase. The new remeshing makes the bubble rise velocity oscillate with a slightly larger amplitude (due to stronger shape deformations), resulting in a slightly lower frequency. Partly, this is due to the volume conservative properties of the new remeshing method, but also the enhanced mesh topology may be of importance. The time-averaged rise velocities do not differ significantly after discarding the transient period of the first 0.2 s, the new remeshing yields 2.82 m/s, whereas the old remeshing gives 2.88 m/s.

The Front-Tracking model with the traditional remeshing technique was used to derive a drag closure for single rising bubbles in an infinite quiescent liquid (Dijkhuizen *et al.*, 2010a). These results were validated against experimental data, and therefore these results provide a good benchmark to assess the performance of the new remeshing implementation. The drag closure that was derived combines a Reynolds dependent part and an Eötvös dependent part:

$$C_D = \sqrt{C_D(\text{Re})^2 + C_D(\text{Eo})^2} \qquad (9a)$$

using an empirically derived correlation for the Eötvös dependent part, and the correlation by Mei *et al.* (1994) for the Reynolds dependent part:

$$C_D(\text{Eo}) = \frac{4\text{Eo}}{\text{Eo} + 9.5} \qquad (9b)$$

$$C_D(\text{Re}) = \frac{16}{\text{Re}} \left(1 + \frac{2}{1 + \frac{16}{\text{Re}} + \frac{3.315}{\sqrt{\text{Re}}}} \right) \qquad (9c)$$

Further details are omitted here, since they are discussed in more detail in Dijkhuizen *et al.* (2010a). The new remeshing technique has also been used to perform simulations using air bubbles in water, and air bubbles in a viscous liquid ($\mu_l = 0.1$ Pa s), using bubble diameters varying from $d_b = 0.1$ mm and 7.0 mm. The extracted drag coefficients for all these cases
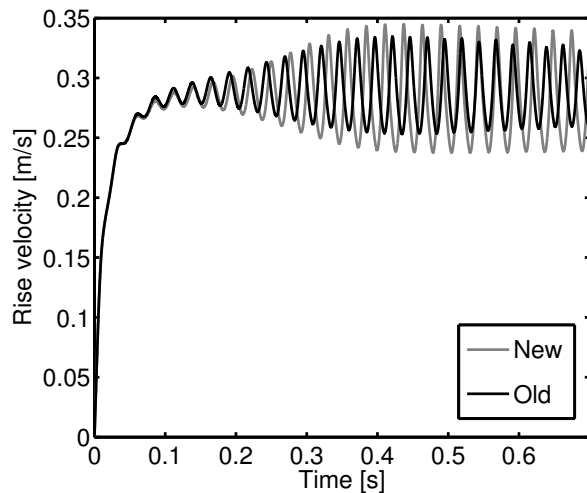

Figure 5: Comparison of the bubble rise velocity vs. time for a 4 mm bubble. While the average rise velocity is consistent in both techniques, the oscillations of the bubble occur at a slightly different frequency.

have been checked to match very well with the previously derived correlation.

Mass transfer

In order to investigate the mass exchange between the gas and liquid phase in a bubble swarm in full detail, a mass transport model was implemented and coupled to the flow field of the Front-Tracking model. The mass transfer model accounts for convection, diffusion, species transfer from the gas to the liquid through the interface, and first-order chemical reaction. This section describes the implementation of the species transport equations into the Front-Tracking framework.

Convection-diffusion equation and boundary conditions

The mass transport equations are solved on a regular Cartesian grid, Γ_s, which is a possibly refined Eulerian mesh directly superimposed onto and aligned with the hydrodynamics grid Γ_h. A refinement factor $\mathscr{R} \in \mathbb{N}$ is used to set the relative mesh size, hence a "parent" hydrodynamics cell contains $\mathscr{R}^3$ "daughter" cells in 3D for solving the mass transfer equations. This technique allows a detailed calculation of the species balance, while keeping the computational time required for the flow solver (especially the expensive pressure-Poisson equation) within limits. Due to the deforming bubble interface and changing flow field properties emerging from the hydrodynamics part of the model, the mass transfer equations must be solved at every time step. The mass balance is given by the convection-diffusion equation on Γ_s as:

$$\frac{\partial c}{\partial t} + \nabla \cdot (\mathbf{u}c) = \mathscr{D}\nabla^2 c - k_1 c + F_s \qquad (10)$$

Here c denotes the concentration in mol/L, $\mathbf{u}$ the velocity, $\mathscr{D}$ the diffusion coefficient in m^2/s, and F_s the source term to enforce the boundary condition at the interface. The diffusion and first order chemical reaction terms are treated implicitly, while the other terms are treated explicitly. The convection term is discretized using the Van Leer scheme.

The solution method uses a projection-correction algorithm to accurately enforce the interface condition, i.e. $c_{\text{interface}} = c_{\text{saturation}}$. First, the equations are solved without a source term F_s^* (Eq. 11) to obtain an intermediate concentration field c^*. The appropriate forcing term can then be calculated after which the correction step follows (Eq. 12).

$$\frac{c^* - c^n}{\Delta t} = -\nabla \cdot (\mathbf{u}^n c^n) + \mathscr{D}\nabla^2 (c^*) - k_1 c^* \qquad (11)$$

$$\frac{c^{n+1} - c^*}{\Delta t} = -\nabla \cdot (\mathbf{u}^n c^n) + \mathscr{D}\nabla^2 (c^{n+1}) - k_1 c^{n+1} + F_s^* \qquad (12)$$

The ICCG matrix solver used to solve the momentum and pressure-Poisson equations in the hydrodynamics part of the code, was also employed here.

Immersed boundary method

An immersed boundary method (IBM) is employed to enforce the interface condition. The species volumetric forcing term F_s^* is determined by calculating the forcing terms for a cell i using the intermediate solution:

$$f_i^* = \frac{Hc_0 - c_i^*}{\Delta t} \qquad (13)$$

where H is Henry's constant (dimensionless) and c_0 is the concentration inside the bubble. The forcing term should

only be accounted for near the interface. The regularization of the forcing term is achieved by using a weighing factor (Eq. 14) from a mapping function (Eq 15), typically using volume weighing (Deen *et al.*, 2004).

$$F_{s,i}^* = w_i \cdot f_i^* \tag{14}$$

$$w_i = \sum_m D\left(\bar{x}_i - \bar{x}_m\right) \frac{V_m}{V_{\text{cell}}} \tag{15}$$

where V_m is the volume associated with a marker m, defined as the marker area A_m multiplied with the characteristic grid cell size:

$$V_m = A_m \sqrt[3]{V_{\text{cell}}} \tag{16}$$

Velocity interpolation

The velocity, required to calculate the convective fluxes of the species, is only known on Γ_h. For $\mathscr{R} > 1$, however, the velocity is required on the refined mesh as well, and an interpolation method is required. It is important to make sure that the resulting velocity field on Γ_s is also divergence free (solenoidal), to prevent local sources or sinks for the concentration and assure that the overall mass balance is intrinsically conserved. Two interpolation techniques that have this property have been implemented:

Piecewise linear interpolation This method, where each direction is interpolated individually, is based on the work of Rudman (1998), who initially described it to perform advection of a colour function on a refined grid. For mass transfer, the method has already been applied in the work of Darmana (2006).

Higher order solenoidal interpolation This method also takes into account the orthogonal translation of the velocity components on the interpolated mesh, describing the velocities on refined cell faces using multiple (one for each direction) second-order polynomials. Details are found in the work of Balsara (2001).

For both methods it has been verified that the initial divergence-free velocity field on Γ_h can be interpolated to Γ_s while maintaining the divergence-free criterium. The latter method shows somewhat smaller errors in our evaluation using synthetic benchmarks, and it will be used as the default interpolation technique.

Initial conditions and boundary conditions

The initial concentration is typically set to zero for cells that contain only liquid, while the concentration inside the bubble is set to the saturation concentration (gas concentration c_0 multiplied by the dimensionless Henry's constant.) To account for cells containing partially gas, the following condition is applied:

$$c_g = c^* = \begin{cases} Hc_0 & \text{if } \phi_{g,i} \geq 0.99 \\ 0 & \text{if } \phi_{g,i} < 0.99 \end{cases} \tag{17}$$

where $i \in \Gamma_s$ denotes the cell on the species grid and $\phi_{g,i}$ the gas fraction in that cell.

Robin (mixed) boundary conditions have been implemented fully implicitly, which can be tuned by setting (α, β, γ) to appropriate values:

$$\alpha c_{\text{wall}} + \beta \left. \frac{\partial c}{\partial x} \right|_{\text{wall}} = \gamma \tag{18}$$

Mass transfer coefficients

The mass transfer between the phases is quantified by calculating the mass transfer coefficient k_L, which can be defined in two different ways;

- Global mass transfer coefficient, integrated over the entire domain. This mass transfer coefficient is calculated using the change of species concentration in the domain before and after the forcing step:

$$k_{L,\text{domain}} = \frac{V_{\text{cell}}}{A_{\text{total}} \Delta t \left(Hc_0 - \langle c \rangle\right)} \sum_{i=0}^{i=n_{\text{cells}}} \left(c_i^{n+1} - c_i^n\right) \tag{19}$$

- Bubble wise, by summing the mass forcing for each marker on a bubble ($F_{s,i}^*$, see Eq. 14), followed by summing the mass transfer for all bubbles. The advantage of this approach is that the mass forcing can be plotted per-marker (for visualisation purposes), and for bubbles rising in swarms, the mass transfer for each bubble can be inspected separately. For a given bubble i, this mass transfer coefficient is given by:

$$k_{L,\text{bubble}} = \frac{V_{\text{cell}}}{A_b \Delta t \left(Hc_0 - \langle c \rangle\right)} F_{s,i}^* \tag{20}$$

Note that the average liquid concentration, $\langle c \rangle$, vanishes for single bubbles rising in a clean, "infinite" liquid. It has been varified that the average of $k_{L,\text{bubble}}$ over all bubbles yields $k_{L,\text{domain}}$.

Validation

Simulations of mass transfer of single rising bubbles have been performed to allow for comparison with correlations from the literature. Many correlations to predict the Sherwood number Sh for single rising bubbles can be found in literature, which are often applicable to a specific regime. An experimentally derived correlation was proposed by Takemura and Yabe (1998) for spherical gas bubbles with a Reynolds number less than 100, and Péclet numbers Pe > 1:

$$\text{Sh} = \frac{2}{\sqrt{\pi}} \left(1 - \frac{2}{3} \frac{1}{\left(1 + 0.09 \text{Re}^{\frac{2}{3}}\right)^{\frac{3}{4}}} \right)^{\frac{1}{2}} \left(2.5 + \sqrt{\text{Pe}}\right) \tag{21}$$

Lochiel and Calderbank (1964) present Eq 22a to account for the Sherwood number of oblate spheroidal bubbles:

$$\text{Sh} = \frac{2}{\sqrt{\pi}} \sqrt{\text{Pe}} \left\{ \frac{2}{3} \left(1 + - \left(\frac{e\chi^2 - \chi \sin^{-1} e}{e - \chi \sin^{-1} e} \right) \right) \right\}^{1/2} \times \\ \frac{2\chi^{1/3} \left(\chi^2 - 1\right)^{1/2}}{\chi \left(\chi^2 - 1\right)^{1/2} + \ln\left[\chi + \sqrt{\chi^2 - 1}\right]} \tag{22a}$$

where $\chi = \frac{\text{major axis}}{\text{minor axis}}$ is the bubble aspect ratio and e the corresponding eccentricity given by:

$$e = \sqrt{\left(1 - \chi^2\right)} \tag{22b}$$

Simulations of a single rising bubble in an infinite liquid, including mass transfer from the gas to the liquid phase, have been performed. The performance of all aspects of the mass

64

transfer model (diffusion, convection, immersed boundary method) have been verified.

The comparison of these results with the correlations is presented in Figure 6. We have determined that the simulations describe the results within 12% of the literature values.
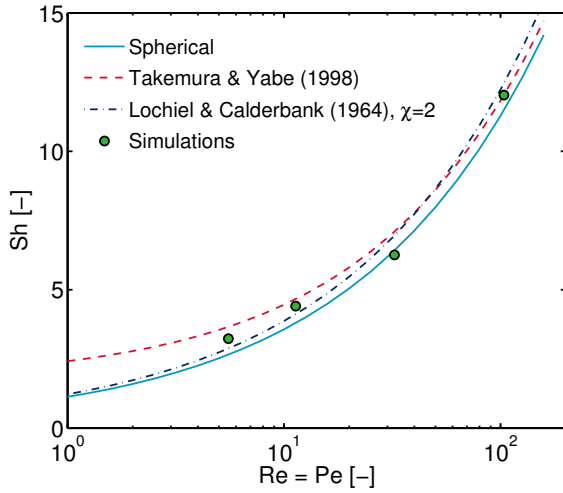

Figure 6: The Sherwood number of a single rising bubble in an infinite, initially quiescent liquid is compared to the exact correlation for flow around a sphere (potential flow) and the correlations of Takemura and Yabe (1998) and Lochiel and Calderbank (1964), the latter plotted for $\chi = 2$

RESULTS

Drag correlation

Simulations have been performed to derive a drag correlation for bubbles rising in a swarm as a function of the gas hold-up (Roghair *et al.*, 2011b).

Simulation settings

The simulation settings (physical parameters) to derive the drag closure are given in this section. Initially, the bubbles are placed randomly throughout the periodic domain. The physical properties of the gas and liquid phases are, for the base case, set up using the values for air bubbles in water. These properties have been varied to investigate the influence of the Eötvös and Morton number. These properties and the resulting Morton and Eötvös numbers are shown in Table 1. For each case, multiple simulations were performed to account for different gas fractions, varying between 5 and 45%. The cases 1–5 were selected to study the influence of the Eötvös number, whilst keeping the Morton number constant. Cases 6–8 are used to study the influence of the Morton number, so we have chosen a set of three Eötvös numbers to which we should compare the results of these cases. For all cases described, the bubble Reynolds number is typically between 150 and 1200.

Although it depends on the exact conditions (viscosity of the liquid phase, bubble diameter, gas fraction), the simulation time is typically about 1.0 s, using a time step of $1 \cdot 10^{-5}$ s. The time-averaged slip-velocity (excluding the initial 0.2 seconds to omit start-up effects) has been used to derive the drag coefficient for each bubble, which is then again averaged to deliver a single drag coefficient.

A drag correlation for bubbles rising in swarms

The relative drag coefficient resulting from the simulations were sorted into series with identical Eötvös numbers. Plotting the drag coefficients, normalised with the drag coefficient on a single rising bubble (Eq. 9a, $C_{D,\infty}$), vs the gas fraction reveals a linear relation with the gas fraction, which starts at $C_D/C_{D,\infty} = 1$ for single rising bubbles, i.e. $\alpha = 0$. The slope of the linear relation varies significantly with the Eötvös number, as shown in Figure 7. A correlation that predicts the drag coefficient of a bubble in a swarm taking into account the Eötvös number and the gas hold-up α can be written as Eq. 23, where the function g incorporating Eo determines the slope of the drag coefficient vs. α.

$$\frac{C_D}{C_{D,\infty}(1-\alpha)} = f(\alpha) = 1 + g(\text{Eo})\alpha \qquad (23)$$

A least squares fit has yielded:

$$\frac{C_D}{C_{D,\infty}(1-\alpha)} = 1 + \left(\frac{18}{\text{Eo}}\right)\alpha \qquad (24)$$

In the range of $1 \le \text{Eo} \le 5$ the correlation performs partic-
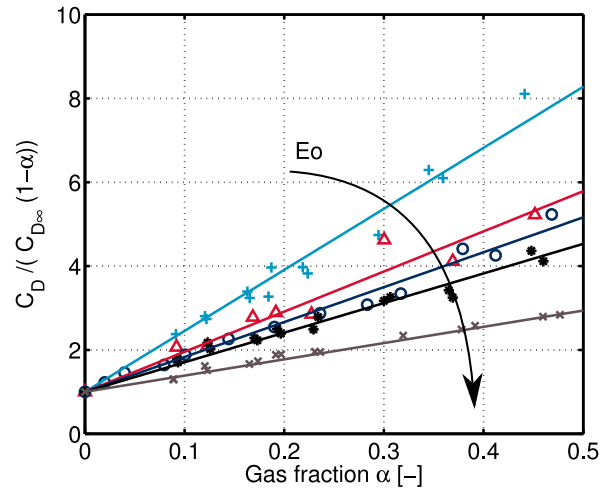

Figure 7: The drag coefficient of a bubble in a swarm, normalized with the drag on a single rising bubbles as a function of the gas fraction, for series of different Eötvös numbers. Legend: +: Eo = 1.21; $\triangle$: Eo = 1.92; $\circ$: Eo = 2.15; $*$: Eo = 2.58; $\times$: Eo = 4.83. Reprinted from Roghair *et al.* (2011b) with permission from Elsevier.

ularly well, describing the drag coefficient found in the simulations within, on average, 1.5% accuracy, while the maximum deviation was found to be 21%. Note that the limit of Eo $\to$ 0 yields an infinitely large drag coefficient, however, it can be expected that at such low Eötvös numbers, a Reynolds number dependency will be found rather than an Eötvös number dependency.

The simulation results shown in Figure 7 have been lumped into data series with identical Eötvös numbers, disregarding the fact that they may have different Morton numbers.

The cases that are lumped together are (see Table 1): 1 with 8 (Eo = 1.21), 4 with 6 (Eo = 2.58) and 5 with 7 (Eo = 4.83). It can be observed in Figure 7, that for all cases, no different trends or otherwise distinctive features due to differences in the Morton numbers can be discerned. In the relatively small range of Morton numbers used in the simulations (between

Table 1: Physical properties for the air-water (base case) simulations. Reprinted from Roghair *et al.* (2011b) with permission from Elsevier.

Case	d_b [mm]	μ_l [Pa s]	ρ_l [kg/m^3]	σ [N/m]	-log(Mo)	Eo	Comment
1	3.0	$1.0 \cdot 10^{-3}$	1000	0.073	10.6	1.21	Air-water
2	6.0	$1.5 \cdot 10^{-3}$	750	0.138	10.6	1.92	
3	4.0	$1.0 \cdot 10^{-3}$	1000	0.073	10.6	2.15	Air-water
4	6.0	$2.0 \cdot 10^{-3}$	1250	0.171	10.6	2.58	
5	6.0	$1.0 \cdot 10^{-3}$	1000	0.073	10.6	4.83	Air-water
6	4.5	$1.5 \cdot 10^{-3}$	950	0.073	9.87	2.58	
7	4.5	$2.0 \cdot 10^{-3}$	1025	0.042	8.67	4.83	
8	4.5	$1.0 \cdot 10^{-3}$	840	0.138	11.35	1.21	

$Mo = 2 \cdot 10^{-9}$ and $Mo = 4 \cdot 10^{-12}$), the Morton number does not affect the drag coefficient.

The derived drag closure, Eq. 24, has been implemented in a discrete bubble model and its performance has been evaluated in Lau *et al.* (2011). The proposed correlation was found to significantly improve the description of the hydrodynamics of bubble columns in comparison to drag coefficients that have been derived using single rising bubbles only. Especially the description of the velocity profiles in the centre part of the column in higher regions has improved with the newly derived correlation.

Bubble induced turbulence

Apart from bubble rise velocities and hence drag coefficients, the front tracking model can also yield information on the liquid characteristics. As bubbles rise, they induce liquid fluctuations which are referred to as pseudo-turbulence. A correct understanding of the pseudo-turbulence is critical for the simulation of bubbly flows, since it influences momentum, heat, and mass transfer rates. The Front Tracking model has been used to study these turbulent fluctuations (Roghair *et al.*, 2011a).

The characteristics of these turbulent fluctuations in the liquid are reflected in the energy spectrum. It has been shown that the energy cascade of pseudo-turbulence behaves differently from homogeneous single-phase turbulence, and hence deserves special attention in large-scale models. Lance and Bataille (1991) studied bubbles rising through an imposed turbulent flow. They measured the energy spectrum of the fluctuations and found a power law scaling with a slope of about $-8/3$, in contrast to the classical $-5/3$ for homogeneous single-phase turbulence.

In the numerical work on pseudo-turbulence by Mazzitelli and Lohse (2009) a slope of $-5/3$ of the energy spectrum was observed. However, in those simulations bubbles were approximated as point-like particles, thus disregarding finite-size effects and capillary phenomena. As Mazzitelli and Lohse (2009) mentioned in their paper, the "wrong" $-5/3$ scaling cannot be the signature of real (experimental) bubble columns.

Indeed, the experimental work of Martínez Mercado *et al.* (2010) found a scaling of the energy spectrum close to -3 for various gas fractions in the very dilute regime. These results were obtained by single-point measurements in flows with gas fractions ranging from $\alpha = 0.8$ to 2.2%, using a phase-sensitive constant-temperature anemometry (CTA) probe.

Simulation settings

Analogue to the experiments due to Martínez Mercado *et al.* (2010), simulations have been performed with the Front Tracking model, hence using finite size bubbles in contrast to the numerics due to Mazzitelli and Lohse (2009). A number of $N_b = 16$ air bubbles in water have been simulated in a fully periodic domain. The bubble Reynolds number is of order O(1000), and the Eötvös number is 2.15.

The simulation time is 4.0 s and we use a time step of $5 \cdot 10^{-5}$ s. Similar to the previous section, transient effects of the initially quiescent liquid and bubbles are excluded by discarding the interval of 0.0—0.2 s for the analysis. Numerical probes have been implemented to record the liquid velocity at different points in the simulation domain. These probes register the phase fraction and the fluid velocity vector in a computational cell at each time step, providing a signal very similar to the signal from the experiments. Hence, these probes are the numerical equivalent to the experimental phase sensitive CTA probe. An array of $3 \times 3 \times 3$ probes has been set up throughout the computational domain.

Turbulent energy spectrum

For the calculation of the energy spectra of liquid fluctuations we follow the method described in Martínez Mercado *et al.* (2010). Since the liquid velocity can only be used if the probe resides in a liquid-filled cell, the velocity signal becomes segmented in time due to passing bubbles. For each probe we calculate the power spectrum density of the segments larger than 256 data points and average over all segments. Finally, an ensemble average over all the 27 probes is done to obtain the final power spectrum.

Figure 8 shows the averaged spectrum of all 27 numerical probes of an $\alpha = 5\%$ simulation together with the experimental data by Martínez Mercado *et al.* (2010). The simulation shows a good agreement, having a slope close to -3 in the frequency range of 20—200 Hz. The scaling frequency range for the simulations is shorter as compared to the experimental case due to the difference in simulation and measurement time. Risso and Ellingsen (2002) pointed out that the power spectra are not influenced by α, based on their experimental findings. In spite of a shorter simulation time and the above discussed convergence problems, in figure 8 we also show the spectra for a case with $\alpha = 15\%$. Due to the smaller signal segments, caused by the smaller distance between the bubbles at higher gas loadings, the -3 scaling range decreases to less than a decade.

Our finding gives additional support to the idea that this particular power law scaling in pseudo-turbulence is related to the wake of the finite-size bubbles. Whether the actual mechanism is dissipiation or transfer should be further investigated. This conclusion lies in line with experiments by Roig and de Tournemine (2007); Risso *et al.* (2008), and theoretical arguments by Lance and Bataille (1991); Risso (2011), who have also indicated the importance of bubbles' wake phenomena.

Mass transfer in bubble swarms

In this section, mass transfer from the gas phase to the liquid phase in a rising bubble swarm is studied using direct numerical simulations. We focus on the industrially relevant case of wobbling air bubbles rising in water. The chemical species that is dissolving has a dimensionless Henry constant of $H = 0.8371$ and a diffusion coefficient of $\mathcal{D} = 10^{-6}$ m/s^2.

Preventing solute accumulation

To prevent the accumulation of species in the domain, and hence to allow for simulation of an indefinite time, the top and bottom boundaries of Γ_s are treated such that the concentration of any inflowing liquid is set to zero, whereas the concentration gradient in the normal direction is gradient free for outflowing fluid. Note that the hydrodynamic equations will still be solved in a regular periodic domain. This way, the domain can be considered as a continuously stirred tank reactor (CSTR), from which the mass transfer coefficient $k_{L,\text{CSTR}}$ can be determined:

$$k_{L,\text{CSTR}} = \frac{\phi_v c_{\text{out}}}{A_{\text{lg}} (c^* - c_{\text{out}})} = \frac{\phi_v \langle c \rangle}{A_{\text{lg}} (c^* - \langle c \rangle)} \qquad (25)$$

Another method of limiting the liquid concentration below the saturation concentration is to incorporate a reaction term into the species balance, so mass transfer to the liquid phase will eventually balance the chemical consumption. In contrast to the method described above, the boundaries are fully
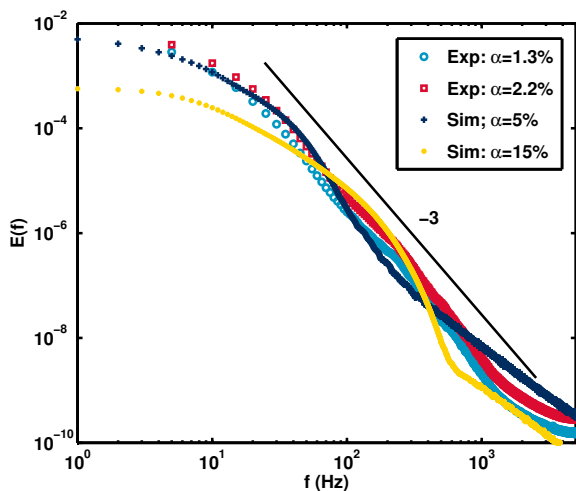

Figure 8: The energy spectra of the simulation is compared to experimental results. For the simulation with $\alpha = 5\%$, a power law close to -3 is observed for nearly one decade starting for frequencies of about 20 Hz till 200 Hz. We also show the simulation case with $\alpha = 15\%$ and with 2 s simulation time, which is not yet fully converged. Reprinted from Roghair *et al.* (2011a) with permission from Elsevier.

periodic, hence there is no inflow or outflow to be considered. When it is assumed that the domain can be represented as a well stirred tank, the domain can be described as an integral mass balance for a batch reactor with mass transfer and reaction in steady state, and the mass transfer coefficient can be determined after rearranging the integral balance:

$$k_{L,\text{batch}} = \frac{k_1 \langle c \rangle}{A_{\text{lg}} (c^* - \langle c \rangle)} \qquad (26)$$

Snapshots of the simulations at $\alpha = 8\%$ and $\alpha = 30\%$, using the CSTR approach and fast and slow chemical reactions, have been provided in the appendix, Figures 11 and 12.

Determining the mass transfer coefficient

The two methods described above have been used to determine the evolution of the mass transfer coefficient for bubbles rising in a swarm as a function of the gas hold-up. For the CSTR case, the time averaged mass transfer coefficient $k_{L,\text{CSTR}}$ as a function of the gas hold-up is given in Figure 9. It is calculated using the forcing terms acting on the interface markers, and using Eq. 25 using both $\langle c \rangle$ and c_{out}. A marginal increase of $k_{L,\text{CSTR}}$ can be discerned when increasing the gas hold-up from 4% to 40%. Extrapolating the trend towards $\alpha = 0.0$ approaches $k_L = 0.016$ m/s, the result for a single rising bubble in an infinite, quiescent liquid. The accuracy of the results strongly decreases for lower gas hold-up ($\alpha < 0.1$), since the number of bubbles, and thus statistics, is limited.
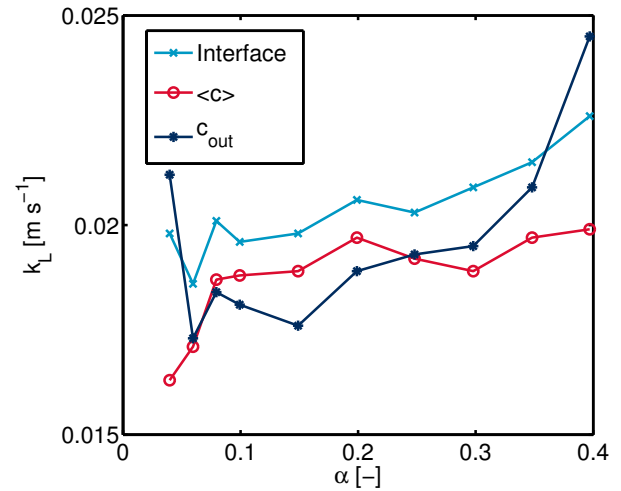

Figure 9: The mass transfer coefficient k_L of bubbles rising in a swarm plotted as a function of the gas hold-up α, determined using fresh inflow boundaries on the top and bottom walls.

The difference between the interface derived mass transfer coefficient and that using the integral balance, is explained by the large fluctuations in the concentration throughout the domain; a closer examination of the liquid concentration in the domain revealed that the standard deviation is of the same order of magnitude as the average concentration. Hence, despite the thorough mixing induced by the bubbles, high and low concentration zones exist throughout the domain, whereas the integral balance assumes a uniform bulk concentration. Rising bubbles encounter both high concentration zones, in the wakes of preceding bubbles, and low concentration zones due to the fresh inflow. The largest portion of the mass transferred through the interface, originates from

the top of the bubble. If this part is surrounded by a high concentration wake of another bubble, the mass transfer rate suddenly decreases.

For the batch reactor approach, two reaction rates have been selected; $k_1 = 50$ s^{-1} and $k_1 = 5$ s^{-1}. The mass transfer coefficient for both cases is shown in Figure 10, using both the integral mass balance (Eq. 26) and the interface forcing terms.
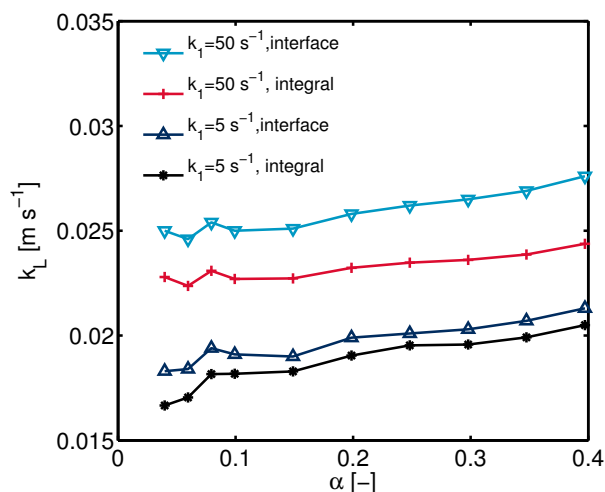

Figure 10: The mass transfer coefficient k_L of bubbles rising in a swarm plotted as a function of the gas hold-up α, determined using a first-order chemical reaction in the liquid phase.

It is observed that the mass transfer coefficient derived from the interface forcing terms is slightly higher than the mass transfer coefficient from the integral balance. The reason for this is similar to that given in the previous section; the concentration field that a bubble actually surrounds, may be quite different from the domain average concentration.

CONCLUDING REMARKS

This work has outlined the implementation of a volume-conserving remeshing technique for the Front Tracking method, and the incorporation of chemical species transport equations. The versatility of the model has been shown by studies focusing on the drag coefficient, bubble induced turbulence and mass transfer for bubbles rising in a swarm.

REFERENCES

BALSARA, D. (2001). "Divergence-free adaptive mesh refinement for magneto-hydrodynamics". *J. Comp. Phys.*, **174**, 614–648.

BUNNER, B. and TRYGGVASON, G. (2002). "Dynamics of homogeneous bubbly flows part . rise velocity and microstructure of the bubbles". *J. Fluid Mech.*, **466**, 17–52.

DARMANA, D. (2006). *On the multiscale modelling of hydrodynamics, mass transfer and chemical reactions in bubble columns*. Ph.D. thesis, University of Twente.

DEEN, N. *et al.* (2004). "Multi-scale modeling of dispersed gas-liquid two-phase flow". *Chem. Eng. Sci.*, **59(8-9)**, 1853–1861.

DEEN, N. *et al.* (2010). *Ullmann's Encyclopedia of Industrial Chemistry*, chap. Bubble Columns. Wiley-VCH Verlag GmbH & Co. KGaA, Weinheim.

DIJKHUIZEN, W. *et al.* (2010a). "DNS of gas bubbles behaviour using an improved 3D front tracking model–drag

force on isolated bubbles and comparison with experiments". *Chem. Eng. Sci.*, **65(4)**, 1415–1426.

DIJKHUIZEN, W. *et al.* (2010b). "DNS of gas bubbles behaviour using an improved 3D front tracking model–model development". *Chem. Eng. Sci.*, **65(4)**, 1427–1437.

FRANCOIS, M. *et al.* (2006). "A balanced-force algorithm for continuous and sharp interfacial surface tension models within a volume tracking framework". *J. Comp. Phys.*, **213(1)**, 141–173.

KUPRAT, A. *et al.* (2001). "Volume conserving smoothing for piecewise linear curves, surfaces, and triple lines". *J. Comp. Phys.*, **172**, 99–118.

LANCE, M. and BATAILLE, J. (1991). "Turbulence in the liquid phase of a uniform bubbly air–water flow". *J. Fluid Mech.*, **222**, 95–118.

LAU, Y. *et al.* (2011). "Numerical investigation of the drag closure for bubbles in bubble swarms". *Chem. Eng. Sci.*, **66**, 3309–3316.

LOCHIEL, A. and CALDERBANK, P. (1964). "Mass transfer in the continuous phase around axisymmetric bodies of revolution". *Chem. Eng. Sci.*, **19**, 471–484.

MARTÍNEZ MERCADO, J. *et al.* (2010). "On bubble clustering and energy spectra in pseudo-turbulence". *J. Fluid Mech.*, **650**, 287–306.

MAZZITELLI, I. and LOHSE, D. (2009). "Evolution of energy in flow driven by rising bubbles". *Phys. Rev. E*, **79(6)**, 066317.

MEI, R. *et al.* (1994). "A note on the history force on a spherical bubble at finite Reynolds number". *Phys. Fluids*, **6**, 418–420.

PIVELLO, M. *et al.* (2013). "A fully adaptive front tracking method for the simulation of two phase flows". *International Journal of Multiphase Flow*.

POPINET, S. and ZALESKI, S. (1999). "A front-tracking algorithm for the accurate representation of surface tension". *Int. J. Numer. Meth. Fluids*, **30**, 775–793.

PROSPERETTI, A. (2002). "Navier-stokes numerical algorithms for free-surface flow computations: an overview". *Drop-surface interaction*, **237**.

RENARDY, Y. and RENARDY, M. (2002). "Prost: A parabolic reconstruction of surface tension for the volume-of-fluid method". *J. Comp. Phys.*, **183(2)**, 400–421.

RISSO, F. (2011). "Theoretical model for k^{-3} spectra in dispersed multiphase flows". *Phys. Fluids*.

RISSO, F. and ELLINGSEN, K. (2002). "Velocity fluctuations in a homogeneous dilute dispersion of high-Reynolds-number rising bubbles". *J. Fluid Mech.*, **453**, 395–410.

RISSO, F. *et al.* (2008). "Wake attenuation in large Reynolds number dispersed two-phase flows". *Phil. Trans. R. Soc. A*, **366**, 2177–2190.

ROGHAIR, I. *et al.* (2011a). "Energy spectra and bubble velocity distributions in pseudo-turbulence: Numerical simulations vs. experiments". *Int. J. Multiphase Flow*, **37(9)**, 1093–1098.

ROGHAIR, I. *et al.* (2011b). "On the drag force of bubbles in bubble swarms at intermediate and high Reynolds numbers". *Chem. Eng. Sci.*, **66**, 3204–3211.

ROIG, V. and DE TOURNEMINE, L. (2007). "Measurement of interstitial velocity of homogeneous bubbly flows at low to moderate void fraction". *J. Fluid Mech.*, **572**, 87–110.

RUDMAN, M. (1998). "A volume-tracking method for incompressible multifluid flows with large density variations". *Int. J. Numer. Meth. Fl.*, **28(2)**, 357–378.
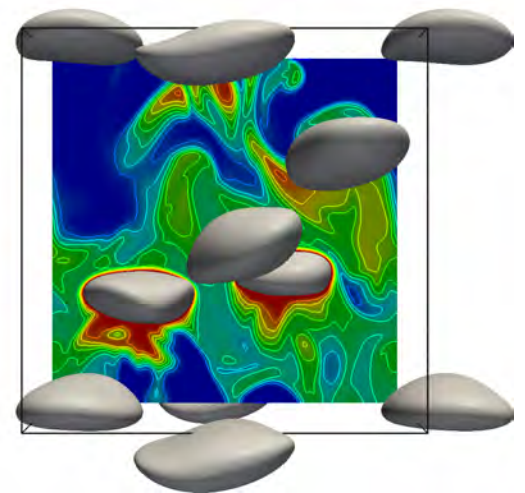
TAKEMURA, F. and YABE, A. (1998). "Gas dissolution process of spherical rising gas bubbles". *Chem. Eng. Sci.*,
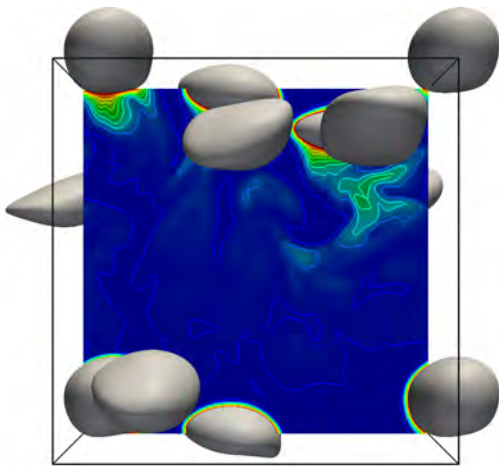
53(15), 2691–2699.

TSIOMBIKAS, J. (2009). "kdtree: A simple C library for working with KD-trees `http://code.google.com/p/kdtree/`".
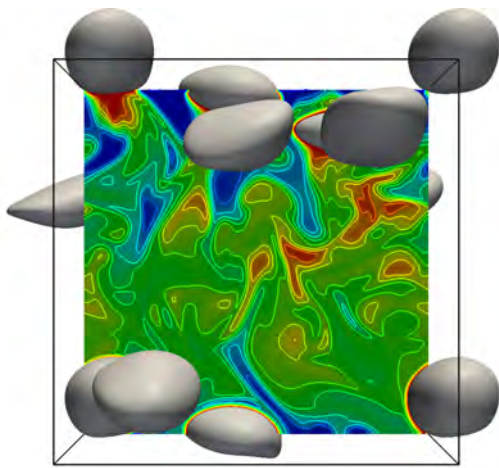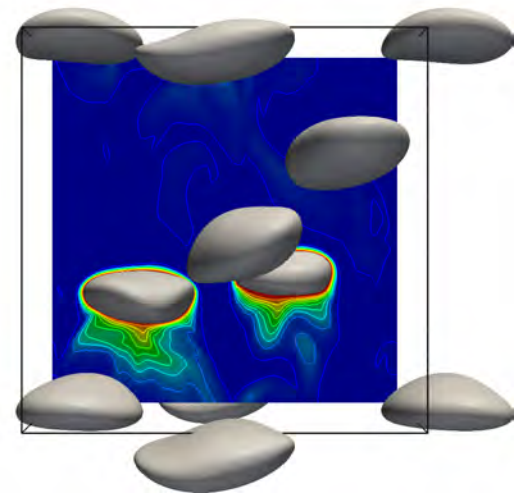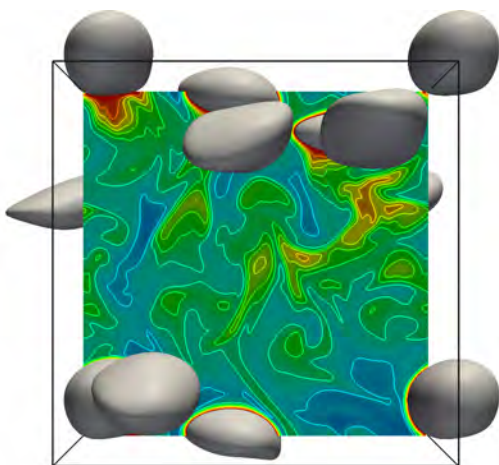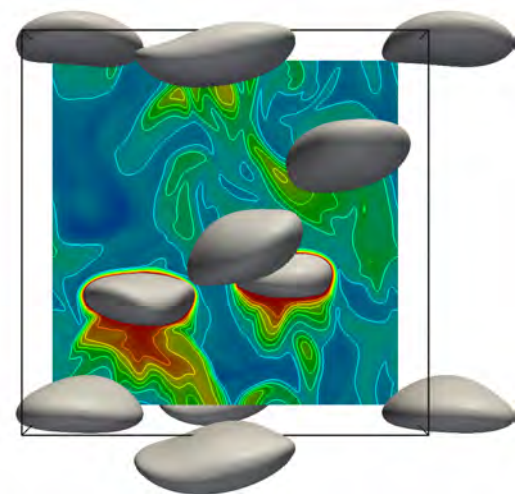
(a) 0.5 s

(b) 1.0 s

(c) 0.5 s

(d) 1.0 s

(e) 0.5 s

(f) 1.0 s

Figure 11: Snapshots of the $\alpha \approx 0.08$ simulations showing the concentration profile in a bubble swarm. From top to bottom, the CSTR approximation, fast reaction and slow reaction are displayed at 0.5 sand 1.0 s. Bubbles on the foreground have been removed for visibility reasons.

(a) 1.0 s

(b) 0.5 s

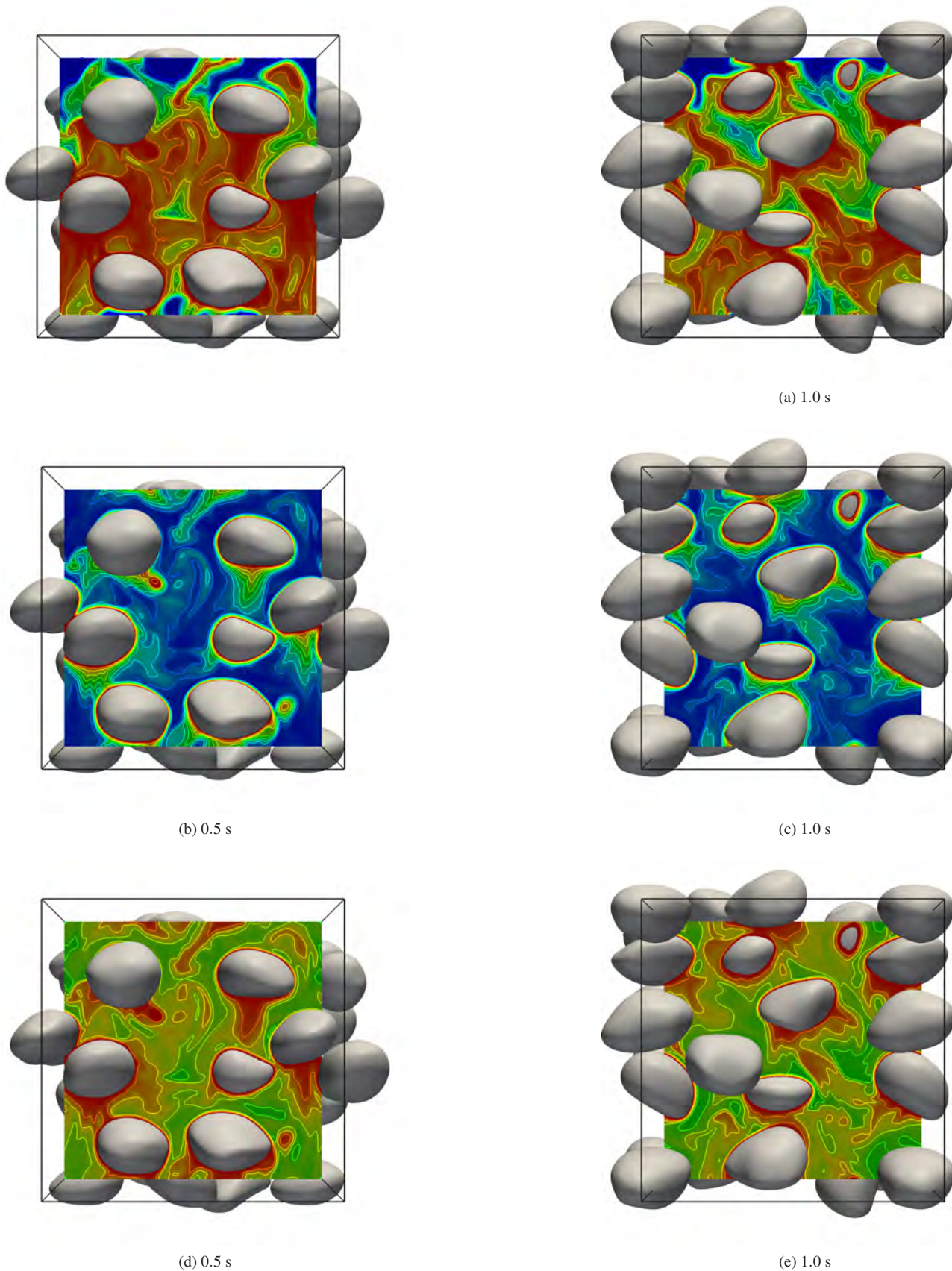(c) 1.0 s

(d) 0.5 s

(e) 1.0 s

Figure 12: Snapshots of the $\alpha \approx 0.30$ simulations showing the concentration profile in a bubble swarm. From top to bottom, the CSTR approximation, fast reaction and slow reaction are displayed at 0.5 sand 1.0 s. Bubbles on the foreground have been removed for visibility reasons.